

# Anti-reflection implementations for terahertz waves

Yuting W. CHEN (✉)<sup>1</sup>, Xi-Cheng ZHANG (✉)<sup>2</sup>

<sup>1</sup> IBM Corporations, Poughkeepsie, NY 12538, USA

<sup>2</sup> The Institute of Optics, University of Rochester, Rochester, NY 14627-0186, USA

© Higher Education Press and Springer-Verlag Berlin Heidelberg 2013

**Abstract** Undesired reflection caused by impedance mismatch can lead to significant power loss and other unwanted effects. In the terahertz regime, anti-reflection method has evolved from simple quarter-wave anti-reflection coating to sophisticated metamaterial device and photonic structures. In this paper, we examined and compared the theories and techniques of several anti-reflection implementations for terahertz waves, with emphasis on gradient index photonic structures. A comprehensive study is presented on the design, fabrication and evaluation of this new approach.

**Keywords** terahertz, anti-reflection, gradient index, photonic structure

## 1 Introduction

The anti-reflection problem in optics is analogous to the impedance matching problem in microwave circuits. RLC circuits, transformers and transmission lines are used to solve the impedance matching problem, whereas in optics a perfect anti-reflection design can be achieved by infinite layers of materials with refractive indices gradually changing between the two medium of interest. The best example is how the atmosphere acts as an antireflection layer to allow sunlight to pass through. In reality, working with limited space and scarcely available materials, it becomes a difficult task to achieve this goal. Research on anti-reflection techniques in the visible wavelengths proliferated over the years, whereas in the terahertz frequency range researchers are still striving to look for the right materials and implementation method.

Take high resistivity silicon as an example—a material suitable for a wide range of terahertz components such as windows, filters and beam splitters because of its high transparency and low dispersion in the entire terahertz range (0.3 to 10 THz). On the other hand, it is associated

with high Fresnel loss due to high index of refraction. With its relative refractive index at 3.42 in the terahertz range, it can be shown that every silicon-air interface on an optical component will induce a 30% loss in power; the use of multiple silicon optics will further reduce available power. This disadvantage plus the already limited power that can be generated by conventional terahertz system severely hinder the use of terahertz technology for many applications. Therefore, there is a pressing need to develop anti-reflection methods to remedy the shortcomings of using multiple silicon components in terahertz systems.

Effective anti-reflection implementation in the terahertz region should cover a broad frequency range. Among various spectroscopy methods, the widely used terahertz time-domain spectroscopy (THz-TDS) technique has a bandwidth from 0.1 to 3 THz. Anti-reflection technique for silicon components used in these systems should have a similar bandwidth in order to be useful at all. Most of the work being reviewed in this paper achieved this requirement. However, as new technologies such as terahertz air-biased-coherent-detection (THz-ABCD) is developed, system bandwidth expands to above 10 THz. In such system, some of the techniques presented here will become obsolete due to their limited bandwidth. To illustrate the progress made in terahertz anti-reflection technique, we will start from single layer quarter-wave coating [1,2] and absorptive metallic coating [3–5], and then move on to more advanced methods such as multi-layer coating [6,7], metamaterial device [8] and sub-wavelength structures [9–11]. In the end, we will focus on gradient index photonic structures, in which we will cover its inception and fabrication as well as its anti-reflection performance evaluated by a THz-ABCD system.

## 2 Developments of anti-reflection implementation in the terahertz frequency range

### 2.1 Quarter-wave coating

Thin-film anti-reflection coating was first discovered by

Lord Rayleigh when he observed that glasses with a tarnished surface can transmit more light than those that are non-tarnished. The principle of quarter-wave coating comes from interference of waves. When the wave reflected from the first surface of the coating has the same amplitude but a phase difference of odd multiple of  $\pi$  with the wave reflected from the second surface, destructive interference will cancel out the two reflected waves and lead to total transmission. To satisfy these requirements, the quarter-wave coating should have an index of  $n = \sqrt{n_{\text{air}} \cdot n_{\text{substrate}}}$  and a thickness of  $t = \lambda/4$ , where  $\lambda$  is the chosen center wavelength of this design.

One of the earliest groups to conduct research on single-layer interference design in the terahertz range is Englert et al. [1]. Their work focused on enhancing transmission around 2.4 THz ( $84 \text{ cm}^{-1}$ ) of aircraft windows used for remote sensing. In the early days, polyethylene is the primary material used to make aircraft windows for remote sensing. However, polyethylene window with a thickness of several millimeters will show noticeable absorption and its low thermal conductivity can cause temperature gradient in the window, which interferes with data measurement. Furthermore, its relatively high emissivity ( $\sim 34\%$ ) in the spectral range makes its disadvantages even more severe. In early 1990s, pure single-crystal silicon was found to be a more suitable material for aircraft windows due to its low absorption. Nevertheless, its high refractive index ( $\sim 3.42$ ) results in high reflection loss and strong Fabry-Perot interference. To solve these issues, researchers applied quarter-wave coating technique on silicon. Since the ideal material with an index of refractive of 1.85 was nonexistent, low-density polyethylene (LDPE) with a relative refractive index of 1.52 was used instead as the coating material. A layer of  $20 \mu\text{m}$  thick of LDPE was put on both sides of the silicon window. The researchers also noted that by using a wedge window of  $0.15^\circ$ , Fabry-Perot interference could be reduced significantly. Figure 1 shows the transmission measurement by terahertz OH-measurement airborne sounder (THOMAS) on quarter-wave coated windows with different wedge angles ranging from  $0^\circ$  to  $0.15^\circ$ .

THOMAS has a rather limited frequency bandwidth. To evaluate the performance of the polyethylene-coated window for a broader spectral range, a smaller sample was made to be tested under a Fourier-transform spectrometer (FTS) with a spectral range from  $60 \text{ cm}^{-1}$  ( $1.8 \text{ THz}$ ) to  $100 \text{ cm}^{-1}$  ( $3 \text{ THz}$ ). In Fig. 2, the transmission measurements taken with FTS were plotted along with model simulation and THOMAS measurement. The simulated transmission of anti-reflection coated plate-parallel window shows severe oscillations whereas that of anti-reflection coated wedge window exhibits a smooth curve over the spectral range. For THOMAS measurement, transmission at  $2.5 \text{ THz}$  is about  $88.7\%$  due to  $4\%$  absorption loss and  $7\%$  reflection loss. FTS and THOMAS

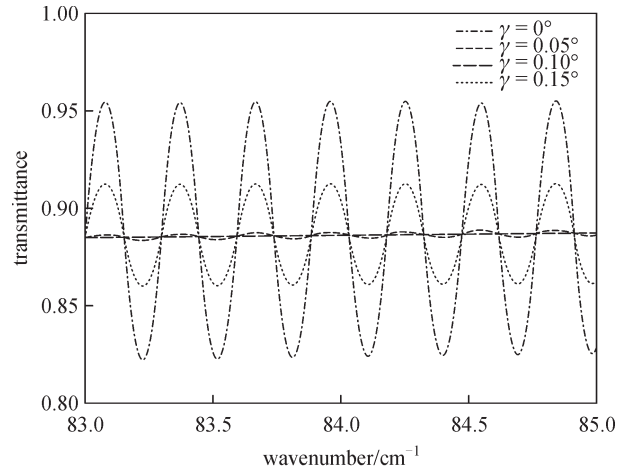


**Fig. 1** Transmittance measurement using THOMAS on quarter-wave anti-reflection coated silicon window with wedge angles of  $0^\circ$ ,  $0.05^\circ$ ,  $0.10^\circ$  and  $0.15^\circ$ , edited for clarity [1]

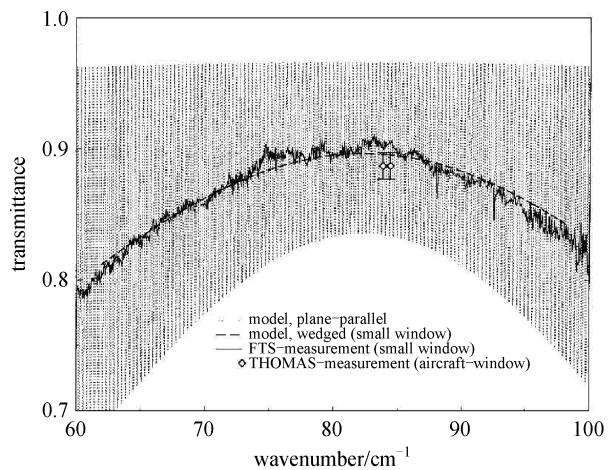


**Fig. 2** Simulated transmissions of model plane-parallel anti-reflection coated silicon window and anti-reflection coated wedge silicon window are plotted in short dash and long dash, respectively. FTS-measurement of small silicon window sample is represented by solid line and THOMAS-measurement of aircraft-window is represented by diamond symbol, edited for clarity [1]

measurements corresponded well with the simulation results, showing no dependence of frequency caused by Fabry-Perot effect.

## 2.2 Absorptive metallic coating

Besides dielectric materials, metallic thin film can also be used to solve the impedance matching problem. Kröll et al. used sub  $10 \text{ nm}$  metallic thin films as anti-reflection coatings for semiconductor substrates, in which the matching layer has a complex refractive index [4]. By tuning the thickness of the matching layer, the condition of

near-zero reflection can be satisfied. There is a major disadvantage of this approach—absorption loss. Figure 3 plots reflection and absorption loss versus sheet conductance of the metallic layer at 1.5 THz for several index mismatch ratio. To achieve zero reflection, a larger index mismatch will require the coating to have higher sheet conductance—hence a thicker layer. The requirement of higher sheet conductance will lead to larger absorption loss of electromagnetic waves.

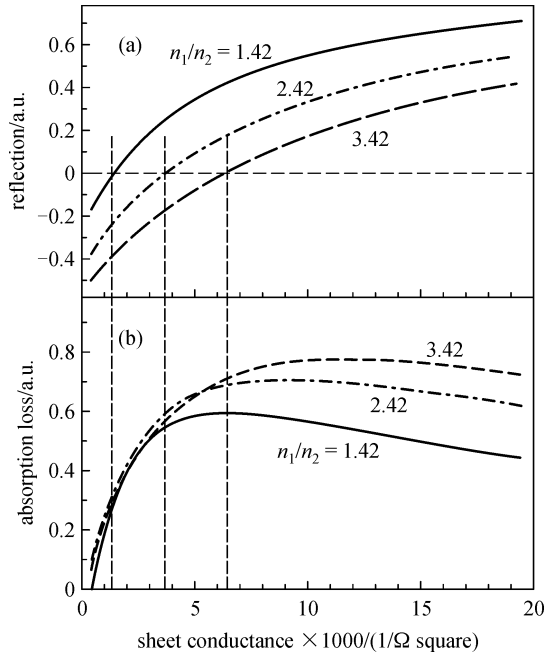


**Fig. 3** Reflection and absorption loss versus sheet conductance at 1.5 THz with index mismatch ratio of 1.42, 2.42 and 3.42 [4]

Despite the drawback of absorption loss, metallic impedance matching layer has the advantage of a broadband anti-reflection profile as compared to quarter-wave dielectric coating, as shown in Fig. 4. This is due to the fact that the phase shift in quarter-wave dielectric coating is proportional to the inverse of wavelength, whereas in metallic matching layer the phase shift is much smaller than one so that the wavelength scaling has far less influence. The researchers then measured two sets of samples using a THz-TDS in transmission mode, which has a spectral range from 0.4 to 4.5 THz.

The first sets of samples are one uncoated high resistivity silicon substrate and one with an 8.3 nm thick chromium coating. The second sets of samples are one uncoated high resistivity GaAs substrate and one with a 44 nm indium tin oxide (ITO) coating. The transmitted time-domain waveforms and the spectral ratio of coated sample normalized to uncoated samples are shown in Fig. 5. From the time-domain waveforms, observation can be made that the reflected secondary pulse disappears for both coated samples, which indicates that reflection is successfully

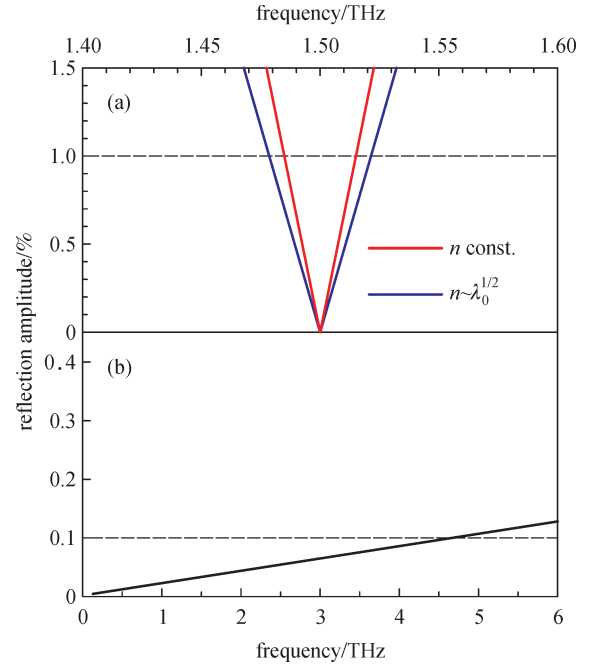


**Fig. 4** Simulated reflection at the GaAs and air interface with (a) quarter-wave dielectric coatings with constant refractive index and frequency dependent refractive index; (b) 16.3 nm thick metallic impedance matching layer [4]

reduced to near zero. However, the amplitude of the main pulse is also reduced. The spectral ratio remains relatively constant around 0.65 throughout the spectral range of the THz-TDS for both sets of samples. This means the anti-reflection performance of the coated samples has a broad bandwidth as depicted in Fig. 4(b). Nonetheless, power loss due to absorption is significant, at around 60%. Therefore this approach may have very limited usage because many applications simply cannot afford to lose more than half its power for using one anti-reflection coated component.

### 2.3 Multi-layer coating

In the visible spectrum, research on multi-layer anti-reflection coatings has seen decades of progress as new materials and techniques became available. Multi-layer coating has the advantage of achieving a broadband anti-reflection effect with a large oblique angle when carefully choosing the refractive index (material) and thickness for each layer [12]. This is a very desirable feature for the application of solar cells where it is crucial to make the efficiency of sunlight capture less dependent on incident angle. Therefore, numerous advancements in multi-layer anti-reflection coating for optical frequencies have been made in recent years. In the terahertz range, multi-layer approach has not been gaining much momentum partly due to the fact that appropriate (non-absorptive, low refractive index) materials are scarce and the required thickness in

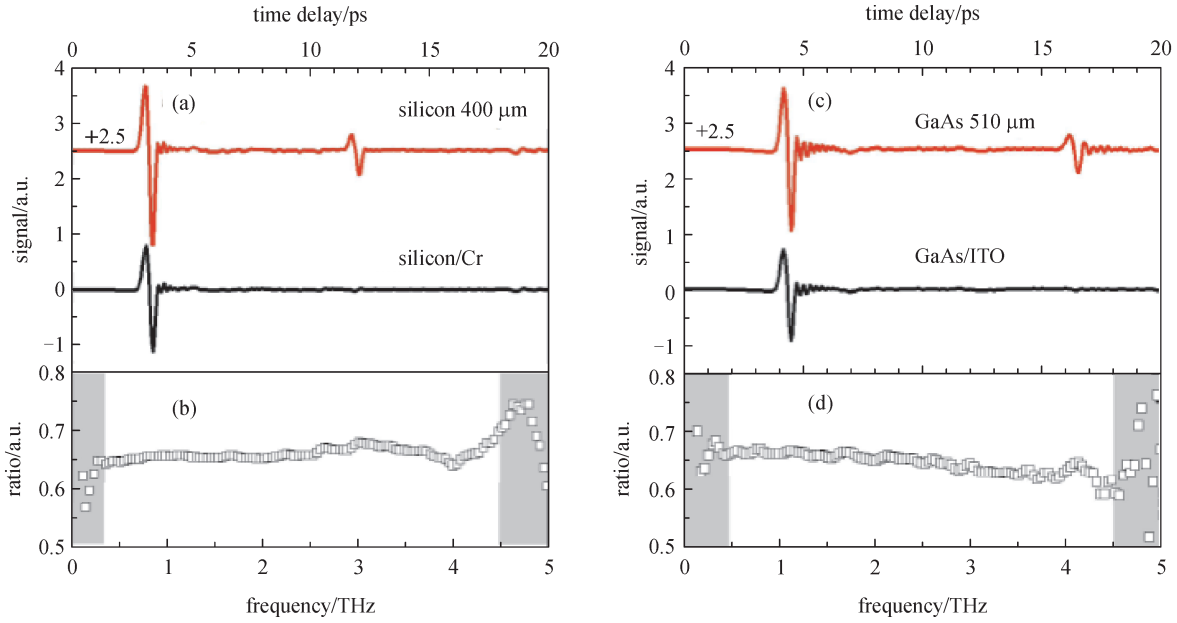


**Fig. 5** THz-TDS transmitted measurements: time-domain waveforms and spectral ratio of uncoated sample versus coated sample of (a, b) high resistivity silicon, 8.3 nm chromium coating and (c, d) high resistivity GaAs, 44 nm ITO coating [4]

the range of tens of microns is difficult to fabricate by standard CMOS process.

Hosako is the first researcher to make multi-layer anti-reflection coating a reality in terahertz frequencies [7]. Using plasma enhanced chemical vapor deposition (PECVD) with silane ( $\text{SiH}_4$ ) and oxygen ( $\text{O}_2$ ) as the source gases, four layers of silicon oxide are deposited onto a germanium substrate. The refractive index of the oxide layer depends on its silicon to oxygen ratio by the equation

$$n_x = \frac{x}{2}n_{\text{SiO}_2} + \left(1 - \frac{x}{2}\right)n_{\text{silicon}}.$$

Figure 6 is a cross-sectional scanning electron microscope (SEM) image showing the four layers deposited on the germanium substrate. Element composition analyzed by energy-dispersive X-ray spectroscopy is also displayed in the figure. To measure the anti-reflection performance of the multi-layer coating, a bare germanium substrate is used as a base reference. Both samples are measured by Fourier transform infrared spectroscopy (FTIR) from  $40 \text{ cm}^{-1}$  (1.2 THz) to  $140 \text{ cm}^{-1}$  (4.2 THz) with a solution of  $4.0 \text{ cm}^{-1}$  (0.12 THz). In Fig. 7, the measured transmittance of the sample is at 100% at  $40 \text{ cm}^{-1}$  and slowly decays to around 60% at  $140 \text{ cm}^{-1}$ , which is the transmittance of bare germanium in this frequency range. Overall, this multi-layer coating has a broadband anti-reflection profile although transmittance is relatively less than optimal.

#### 2.4 Metamaterial device

Terahertz split ring resonators (SRRs) were first designed

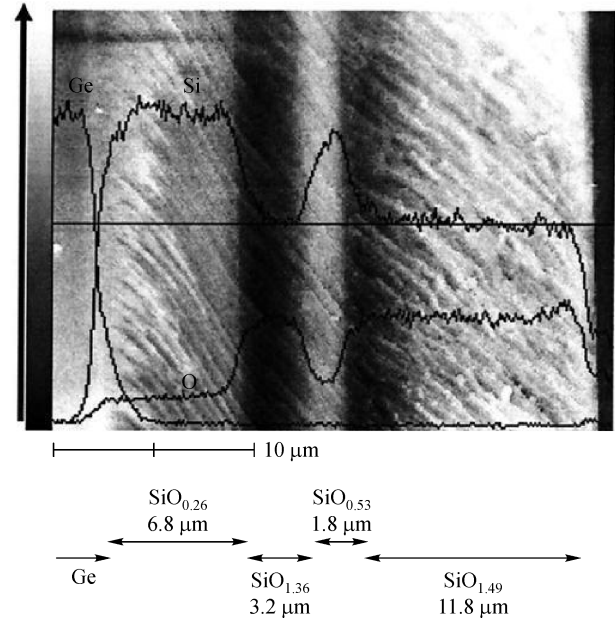


**Fig. 6** SEM image showing cross-section of the germanium substrate with four layers of silicon oxide deposited as anti-reflection coating, edited for clarity [7]

to control and manipulate radiation [8]. Due to the fact that real dielectric constant of the device can be tuned by an applied voltage, such device can also be used for anti-reflection purpose. In that particular research, Chen et al. investigated an array of SRRs as anti-reflection coating on a GaAs substrate.

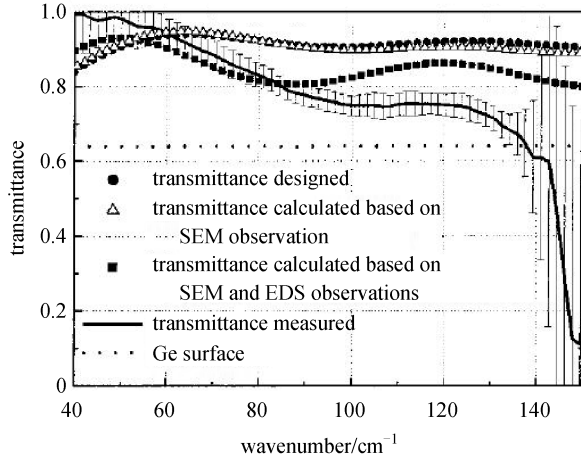


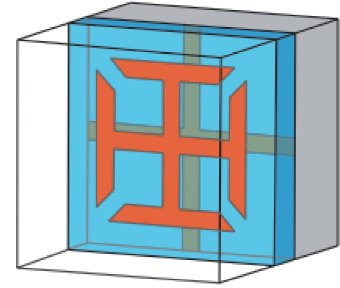
**Fig. 7** Transmittance of multi-layer silicon oxide coating on germanium substrate: solid circle is designed value, triangle is calculated value from SEM measurement, solid square is calculated value base on SEM measurement and EDS analysis, and solid curve is measured value under FTIR, edited for clarity [7]

The metamaterial device is composed of a metal mesh layer separated by a polyimide spacer to a layer of  $36\ \mu\text{m}$  by  $36\ \mu\text{m}$  SRRs, and the period of the array is  $46\ \mu\text{m}$ . A unit cell of the device is shown in Fig. 8(a). Measured reflectance and transmittance of the device at normal incidence are plotted along with that of a GaAs substrate, as shown in Fig. 8(b). Enhanced transmission is observed from roughly 0.9 to 1.3 THz, demonstrating anti-reflection effect. However, there is an overall loss about 10%.

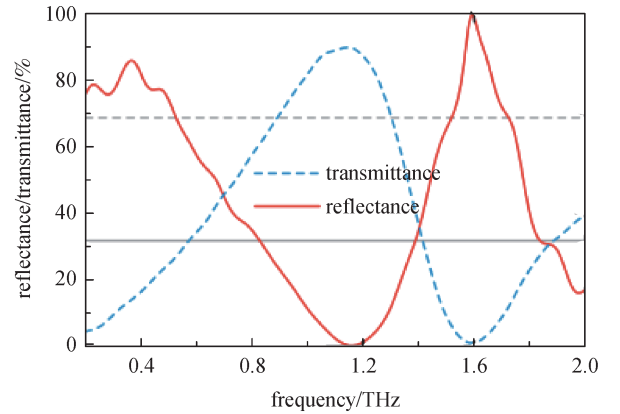
Furthermore, the researchers measure reflectance at various incident angles for both transverse magnetic (TM) and transverse electric (TE) polarization. Reflectance of the device has a minimum near 1.2 THz, and that minimum value remains under 1% for TM polarization for all measured incident angle, comparing to 27.2% at  $20^\circ$  and 8.7% at  $60^\circ$  for GaAs substrate. However, for TE polarization it steadily increases to 10.9% when incident angle changes from  $20^\circ$  to  $60^\circ$ , comparing to 34% at  $20^\circ$  and 56% at  $60^\circ$  for GaAs substrate. The results are shown in Fig. 9. Despite the narrow bandwidth of its anti-reflection performance, this metamaterial device is well suited for applications where large incident angle is inevitable.

### 2.5 Sub-wavelength surface relief structures

Sub-wavelength surface relief structures are also known as “moth-eye” structures. Mimicking the periodic arrays of small protuberance on moth eye, these structures were found to reduce reflection and enhance transmission. By tuning the period of these arrays, they can be implemented for any spectral range. Advancements in semiconductor IC fabrication have made it feasible to produce nano-scale sub-wavelength surface relief structures for the visible



(a)



(b)

**Fig. 8** (a) A unit cell of the metamaterial device; (b) reflectance and transmittance of the device measured under THz-TDS comparing with that of GaAs substrate [8]

range. However, arrays with size of tens of microns for the terahertz range are prohibitively expensive and time-consuming to fabricate using standard IC fabrication techniques.

Using mechanical machining techniques, two groups of researchers had implemented sub-wavelength surface relief structures in the terahertz range [9,10]. Brückner et al. [9] fabricated triangular grooves on both sides of a Topas plastic plate with a period of  $100\ \mu\text{m}$  and a depth of  $200\ \mu\text{m}$  by single point diamond turning process; enhanced transmission was observed below 0.5 THz. Similar structures of a  $74\text{-}\mu\text{m}$  period and a  $55\text{-}\mu\text{m}$  depth on high resistivity silicon were made by Kuroo et al. [10] with a dicing blade; in comparison its anti-reflection profile has a boarder bandwidth, from 0.1 to 1.5 THz, due to a smaller structure period.

We published our work on micro-pyramid surface relief structures in 2009 [11]. Closely packed micro-pyramid arrays were fabricated on high resistivity silicon substrate utilizing crystallographic wet etch. An SEM image of an array with  $45\text{-}\mu\text{m}$  period is shown in Fig. 10. To understand the anti-reflection effect of these micro-pyramid arrays, we can think of the structures as composition of many layers whose relative refractive index continuously changing from 1 (air) to 3.42 (silicon). Difference in refractive index between adjacent layers is

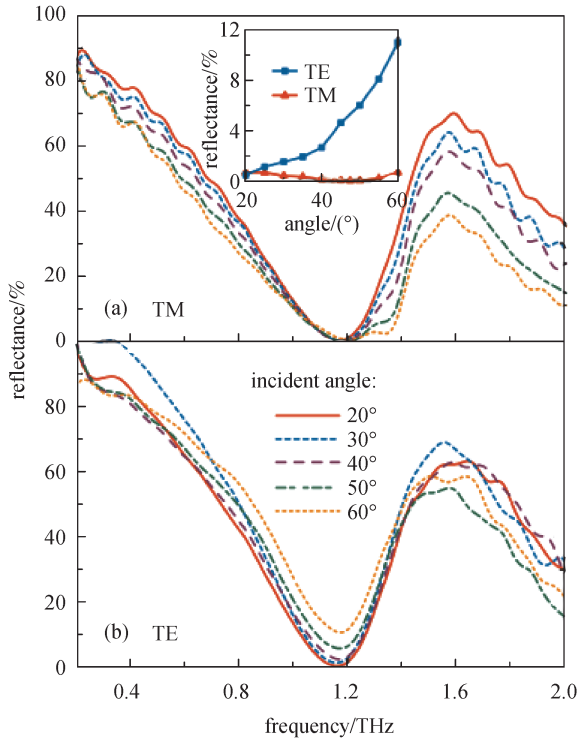


**Fig. 9** Measured reflectance of (a) TM polarization and (b) TE polarization for incident angles from  $20^\circ$  to  $60^\circ$  [8]

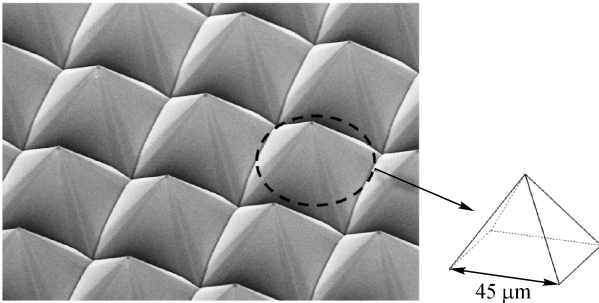


**Fig. 10** SEM image of a micro-pyramid array with a  $45\text{-}\mu\text{m}$  period [11]

quite small; therefore reflection resulting from index mismatch is also small.

A series of micro-pyramid arrays with period from  $30$  to  $110\text{ }\mu\text{m}$  were evaluated under THz-TDS. Measured reflectivity of all the samples is plotted in Fig. 11. For sub-wavelength structures to work as designed, its period has to be much smaller than intended wavelengths. As seen in Fig. 11, when the period of the arrays approaches the order of wavelength in the terahertz range, diffraction occurs and consequently hampers anti-reflection performance. Micro-pyramid arrays with a  $30\text{ }\mu\text{m}$  period has a minimum of  $7\%$  at  $2.5\text{ THz}$  and an anti-reflection bandwidth from  $0.1$  to  $3.2\text{ THz}$ , broadest among all samples and previously published work on surface relief

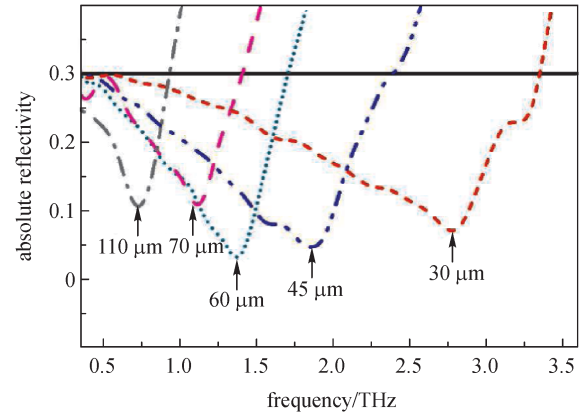


**Fig. 11** Measured reflectivity of micro-pyramid arrays with period of  $30$ ,  $45$ ,  $60$ ,  $70$  and  $110\text{ }\mu\text{m}$  [11]

structures in the terahertz range. One drawback of micro-pyramids fabricated by wet etch is that the apex angle is determined by substrate's crystal structure, thus the base to height ratio cannot be modified to improve anti-reflection performance.

### 3 Gradient index photonic structures

#### 3.1 Design inception

Inspired by Egyptian Pyramids of which the structures are constructed by many steps, we transform the micro-pyramid into a three-layer structure so that the period and the height can be individually tuned to achieve optimal anti-reflection performance for wavelength of interest. Figure 12 shows a 3-D prototype of this three-layer structure. Applying gradient index anti-reflection theory [12,13], each layer will have a specific requirement on refractive index and thickness. The parameters are obtained from a Gaussian profile with a minimum of  $1$  (relative refractive index of air) and a maximum of  $3.42$  (relative refractive index of silicon). The profile is then divided into three sections and a discretization process is used to find the refractive index and thickness of each section (layer) for the best overall performance. The calculated parameters are shown in Table 1. Total thickness of the structure is comparable to intended wavelength in order to ensure anti-reflection effectiveness. Reflectance of the designed structure versus unit wavelength is shown in Fig. 13, reflectance of blank silicon is also plotted for comparison.

To attain high aspect ratio, we use dry reactive ion etching (DRIE) for fabrication. During early stage of prototyping, we realize that etching pillars on silicon substrate is not the best way to implement the three-layer design. First of all, photolithography becomes very challenging after the first layer when we try to pattern on

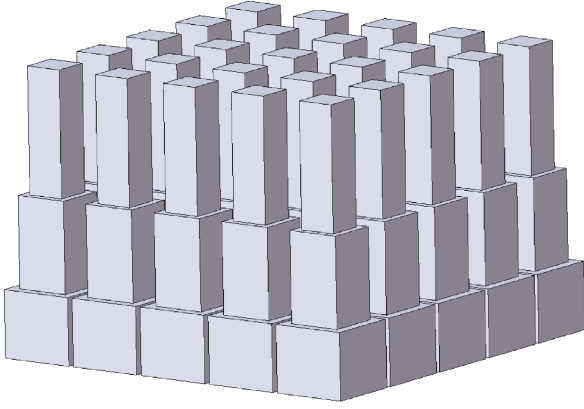


**Fig. 12** 3-D prototype of three-layer pyramid structure

small islands. Moreover, pillars are prone to damage since they are free standing on a flat surface. To overcome these issues, our original three-layer structure evolves to a new design where holes instead of pillars are etched on the silicon substrate. This is shown in Fig. 14. The fabrication process starts with the layer closest to the substrate and works bottom-up. Since for every photolithography process we will have a connected flat surface to work on, the photoresist mask quality can be greatly improved for the upper two layers. Furthermore, the new structure forms a mesh network such that it is more robust than the previous pillar design.

When we etch bulk silicon, the refractive index of the substrate is altered. A simple formula to describe the refractive index of a periodic etched square pattern in bulk material is derived by Kadlec et al. using a circuit model [14]. As illustrated in Fig. 15(a), a layer of silicon pillars are divided into unit cells where  $x_1$  and  $x_2$  represent the two width dimensions of a pillar and  $\varepsilon$  represents the permittivity of silicon. This setup is then translated into a circuit in Fig. 15(b) where silicon pillar is considered as a capacitor, and it is in series with the air gap capacitor to its right and then in parallel with the air gap capacitor at the top. An SEM image of such periodic etched layer is shown in Fig. 15(c).

A capacitor is defined as

$$C = \frac{\varepsilon A}{d}, \quad (1)$$

in which  $\varepsilon$  is permittivity of the dielectric material,  $A$  is the area of the conductive plate and  $d$  is the distance between the conductive plates. Since all capacitor in the model has

the same height,  $A$  can be simplified as  $x_1$  and  $d$  can be replaced by  $x_2$ . Therefore, the capacitors in this model are formulated as

$$C_1 = \frac{\varepsilon x_1}{x_2}, \quad (2)$$

$$C_2 = \frac{x_1}{1-x_2}, \quad (3)$$

$$C_3 = 1-x_1. \quad (4)$$

The overall capacitor is

$$C = \frac{1}{\frac{1}{C_1} + \frac{1}{C_2}} + C_3. \quad (5)$$

Rearranging the formula, one can find that the permittivity of this overall capacitor is

$$\varepsilon_1 = 1 + \frac{x_1 x_2}{\varepsilon - 1 - x_2} = n_1^2, \quad (6)$$

in which  $n_1$  is the effective refractive index of the layer.

Since we have changed our design from silicon pillars to holes, the corresponding unit cell is also transformed, as illustrated in Fig. 16. From the new unit cell model, we can formulate the capacitors as following:

$$C_1 = \frac{x_1}{x_2}, \quad (7)$$

$$C_2 = \frac{\varepsilon x_1}{1-x_2}, \quad (8)$$

$$C_3 = \varepsilon(1-x_1). \quad (9)$$

The overall capacitor has the same form as Eq. (5), which translates into the overall permittivity being:

$$\varepsilon_1 = \frac{\varepsilon x_1}{\varepsilon x_2 + 1 - x_2} + \varepsilon(1-x_1) = n_1^2. \quad (10)$$

Since our etching profile is square, the overall permittivity can be simplified to

$$\varepsilon_1 = \frac{1}{1 + \frac{1-x}{\varepsilon x}} + \varepsilon(1-x) = n_1^2. \quad (11)$$

To visualize this equation, we plot the relative refractive index  $n_1$  versus etch dimension  $x$  in Fig. 17. On the other

**Table 1** Design parameters of three-layer structure from gradient index anti-reflection theory

layer	1 (air)	2	3	4	5 (silicon)
effective index of refraction	1.0	1.55	2.25	2.95	3.42
thickness (per unit wavelength)	–	0.3156	0.225	0.172	–

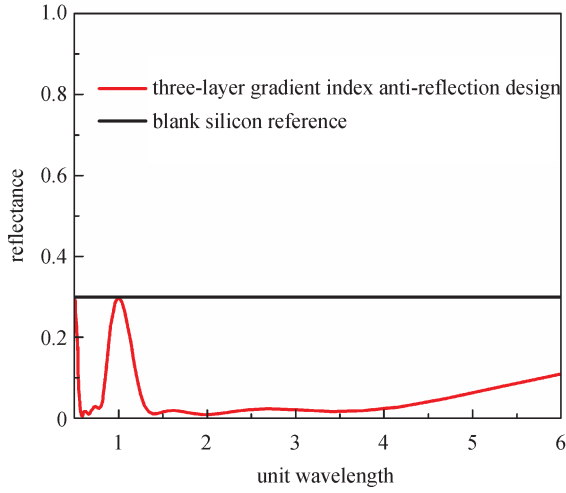


**Fig. 13** Reflectance of designed three-layer structure and blank silicon versus unit wavelength

hand, we etch a layer of periodic square holes with a period of  $20\ \mu\text{m}$ , a depth of  $21.8\ \mu\text{m}$  and a width of  $15.52\ \mu\text{m}$  to verify our formulation. A cross-section SEM image of the etched layer is shown in Fig. 18. Using Eq. (11) with  $\varepsilon = 3.42^2$  and  $x = 15.52/20 = 0.776$ , the calculated refractive index of this profile is 1.90. We then use a THz time-domain spectrometer to measure the time shift between etched area versus unetched area. The effective refractive index of the etched area can be calculated as

$$n_{\text{etched}} = n_{\text{silicon}} - \Delta n, \quad (12)$$

where

$$\Delta n = \frac{tv}{d}. \quad (13)$$

In Eq. (13),  $t$  is the measured time shift,  $d$  is the etched layer depth and  $v$  is the speed of light. Figure 19 shows the time shift measured by THz-TDS, in which the delay between the terahertz waveform peaks is  $0.11\ \text{ps}$ . With  $t = 0.11 \times 10^{-12}\ \text{s}$ ,  $v = 3 \times 10^8\ \text{m/s}$ ,  $d = 21.86\ \mu\text{m}$  and  $n_{\text{silicon}} = 3.42$ ,

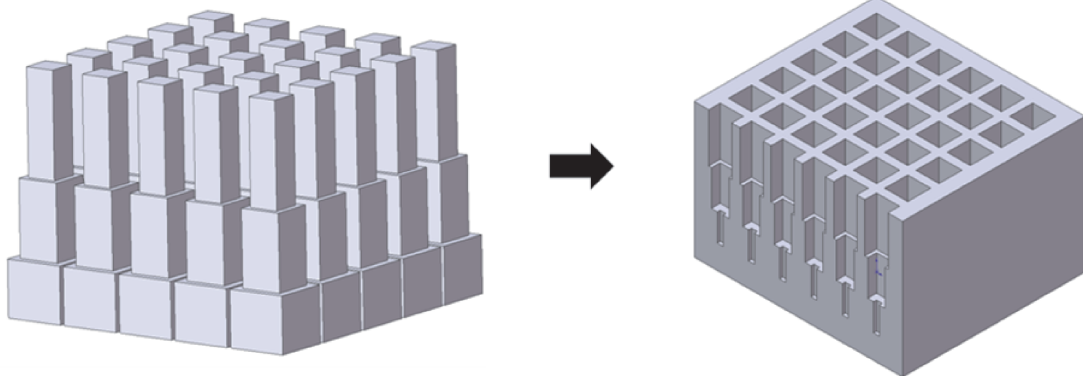


**Fig. 14** Transformation of three-layer photonic design

the measured relative refractive index of the profile is 1.91. The excellent correspondence of the expected value and the measured value confirms that our formulation of Eq. (11) is accurate and this equation will be used later on to calculate periodic hole dimension for fabrication.

### 3.2 Structure simulation

Our next step is to choose a suitable unit wavelength, which will determine the thickness of each layer in the structure. To accomplish this goal, we create a simulation model and use it to calculate the overall reflectance and transmission profile of any dielectric multi-layer structures in the terahertz range. The model is based on transfer matrix theory under the condition of normal incidence. For a three-layer structure between air and silicon, as shown in Fig. 20, each layer as well as the air and the silicon medium can be represented by a propagation matrix,

$$\mathbf{P}_{(i)} = \begin{bmatrix} e^{-jn_i kd_i} & 0 \\ 0 & e^{jn_i kd_i} \end{bmatrix}, \quad (14)$$

where  $n_i$  is the relative refractive index of layer  $i$  and  $d_i$  is the layer thickness. The boundary between any two adjacent layers can be represented by a transmission matrix,

$$\mathbf{T}_{(i)} = \frac{1}{2n_{i+1}} \begin{bmatrix} n_{i+1} + n_i & n_{i+1} - n_i \\ n_{i+1} - n_i & n_{i+1} + n_i \end{bmatrix}, \quad (15)$$

where  $n_{i+1}$  and  $n_i$  are the relative refractive indices of two neighboring layers. The overall transmission matrix representing a three-layer device in between air and silicon can be written as

$$\mathbf{M} = \mathbf{P}_{(5)} \prod_{i=1}^4 \mathbf{T}_{(5-i)} \mathbf{P}_{(5-i)}, \quad (16)$$

where  $\mathbf{P}_{(5)}$  is the transmission matrix of silicon medium,  $\mathbf{P}_{(1)}$  is the transmission matrix of air medium. Matrix  $\mathbf{M}$  can also be written as

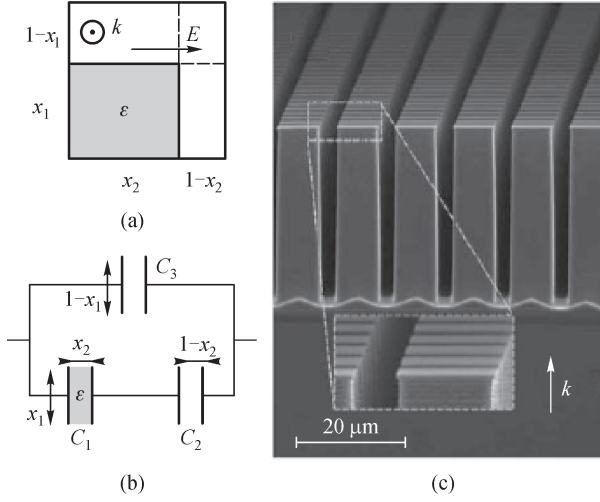


**Fig. 15** (a) Schematic of a unit cell inside a periodic etched layer; (b) circuit model used to describe the unit cell; (c) SEM image of such periodic etched layer [14]

$$\mathbf{M} = \begin{bmatrix} A & B \\ C & D \end{bmatrix}, \quad (17)$$

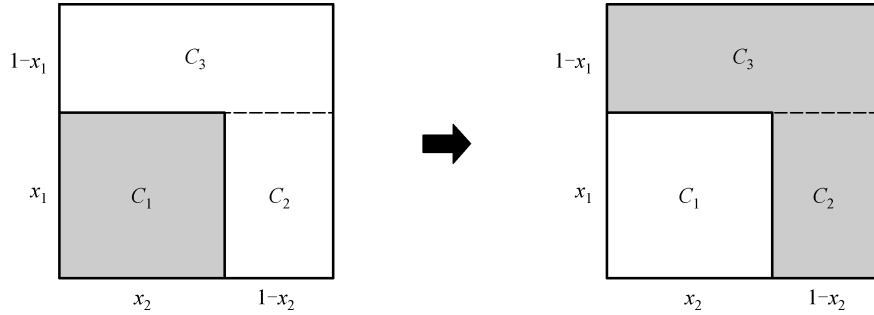


**Fig. 16** Transformation of unit cell from periodic pillars to periodic holes

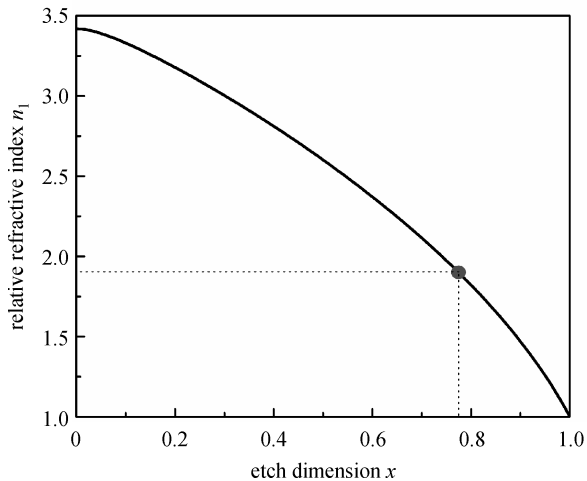


**Fig. 17** Relative refractive index of an etched periodic square hole layer versus etch dimension

which can be converted into a scattering matrix  $\mathcal{S}$  [15].

$$\mathcal{S} = \frac{1}{D} \begin{bmatrix} AD-BC & B \\ -C & 1 \end{bmatrix} = \begin{bmatrix} t_{12} & r_{21} \\ r_{12} & t_{21} \end{bmatrix}. \quad (18)$$

In scattering matrix  $\mathcal{S}$ ,  $t_{12}$  is the transmission of wave from medium 1 to medium 2 and  $r_{21}$  is the reflection of wave from medium 2 to medium 1.

Using this simulation model, we set the refractive index of the three layers based on Table 1. Unit wavelengths of 28, 39, and 51  $\mu\text{m}$  are chosen, which have corresponding total structure thicknesses of 20, 28 and 36  $\mu\text{m}$ , respectively. The layer thickness of air and silicon in our simulation are set to a value much larger than unit wavelength such that no interference will be observed. The simulated frequency is set from 0.1 to 8 THz. To illustrate the effect of structure thickness on anti-reflection performance, we plot the simulation reflectance profile in Fig. 21 for three different total structure thicknesses. We observe that as structure depth increases, anti-reflection performance will shift to higher wavelength (lower frequency). This is due to the fact that reflectance profile from gradient index design is based on unit wavelength and the change in

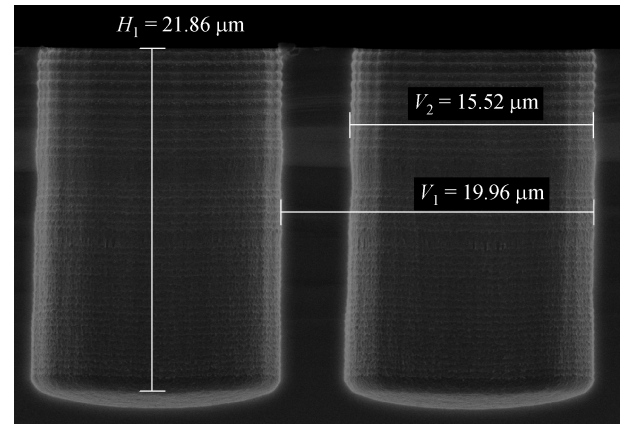


**Fig. 18** Cross-section SEM image of an etched layer

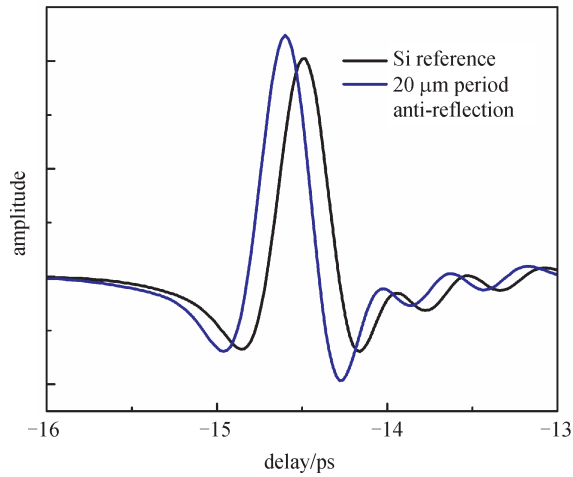


**Fig. 19** THz-TDS measured waveforms of unetched area and etch area on silicon substrate

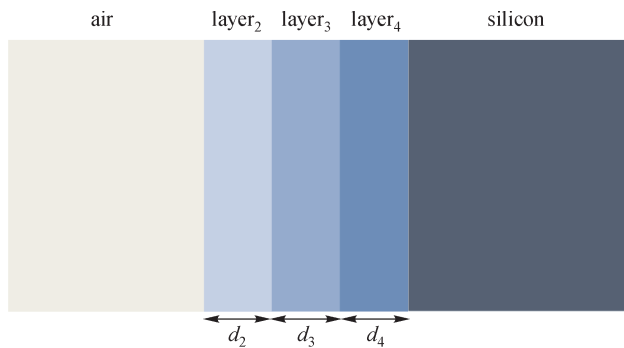
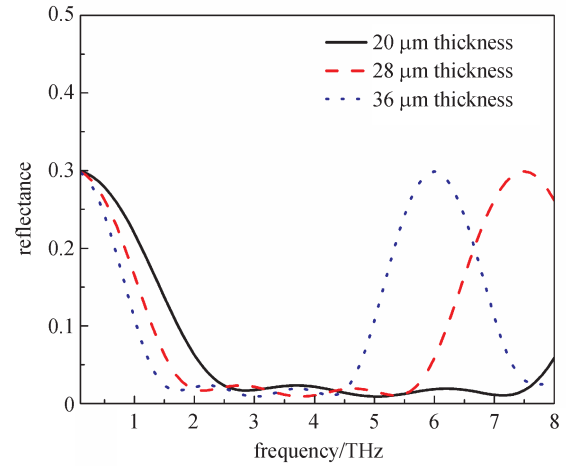


**Fig. 20** Three-layer dielectric system between air and silicon

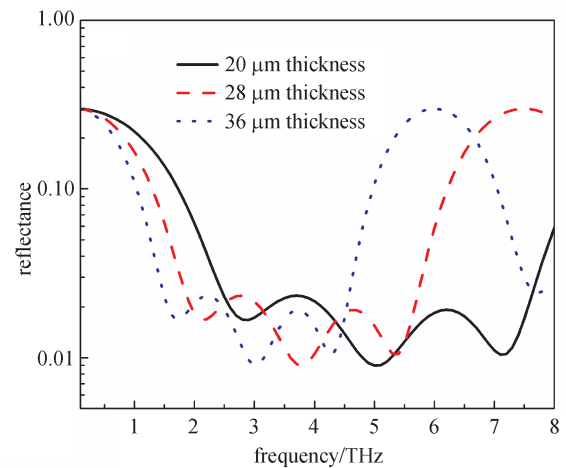
layer thickness means change in the chosen unit wavelength. Therefore, as chosen unit wavelength increases, center wavelength of applicable antireflection effect also shifts up. Since structure with a thickness of  $20\ \mu\text{m}$  has the widest bandwidth, we select it for our fabrication process. For structure period, we choose 15 and  $20\ \mu\text{m}$  in order to delay occurrence of diffraction to high frequencies. Complete fabrication parameters are listed in Table 2.

### 3.3 Structure fabrication

Fabrication of the three-layer gradient index anti-reflection structure fully utilizes standard CMOS fabrication equipments. The process cycle is illustrated in Fig. 22. Three photomasks are needed to pattern the designed features. The first fabrication cycle will start with the smallest feature, which is the layer closest to silicon substrate. This can insure subsequent cycle will have enough surface area to make contact with photo-mask during the lithography step. Due to variations in feature size and layer depth in each cycle, process recipe such as exposure time, etching time will need to be tuned accordingly to achieve desired results.



(a)



(b)

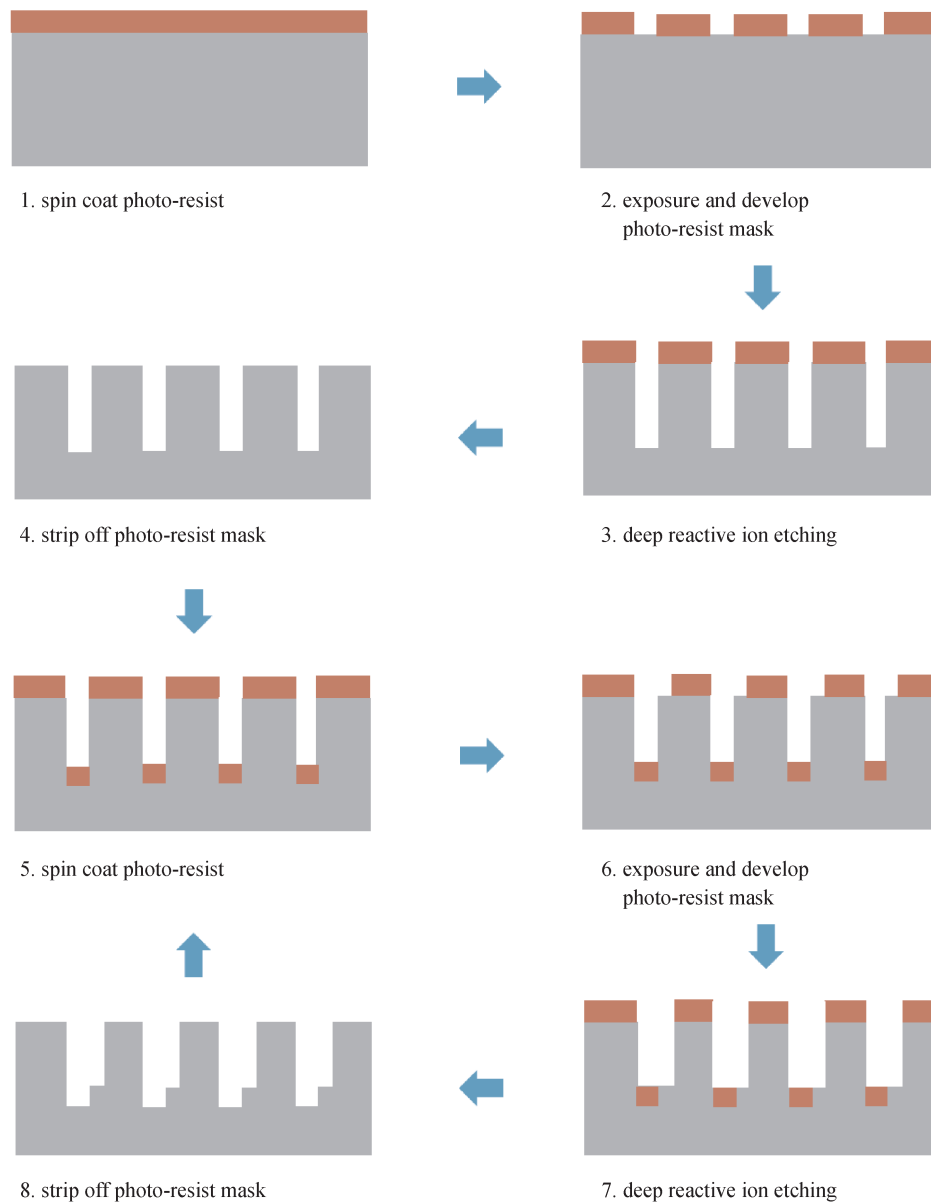
**Fig. 21** Simulated reflectance versus frequency of three-layer gradient index structure with total thickness of 20, 28 and  $36\ \mu\text{m}$  in (a) linear scale and (b) log scale

Since our design involve etching deep trenches in silicon substrate, Bosch process used in deep reactive-ion etching (DRIE) is necessary to produce such features. Bosch process is composed of alternating etching and passivation steps. For silicon substrate,  $\text{SF}_6$  gas is used as etchant and  $\text{C}_4\text{F}_8$  gas is used as passivator. The etching step is an isotropic process, which only lasts a few seconds; then the passivation step will kick in and run for a few seconds. Owing to the fact that many small steps of isotropic etch are taken, the sidewall of the trench will have scalloping characteristic. The scalloping of sidewall can be smoothed by reducing the etch time for each step. Along with Bosch process, the substrate is also chilled to a low temperature and one-minute cool-down steps are taken for every minute of etching. This is to prevent overheating, which can cause fast dissipation of the photo-resist mask and lead to failure of the etching process.

SEM image of a  $20\text{-}\mu\text{m}$  period structure is shown in Fig. 23. The smallest feature is the layer closest to silicon

**Table 2** Complete fabrication parameters of three-layer structures

layer	1 (air)	2	3	4	5 (silicon)
refractive index	1.0	1.55	2.25	2.95	3.42
layer height	–	8.9 $\mu\text{m}$	6.3 $\mu\text{m}$	4.8 $\mu\text{m}$	–
air ratio/%	100	77.44	42.25	10.89	0
hole dimension ( $\lambda = 20 \mu\text{m}$ )	–	17.6 $\mu\text{m}$ ×	13.0 $\mu\text{m}$ ×	6.6 $\mu\text{m}$ ×	–
hole dimension ( $\lambda = 15 \mu\text{m}$ )	–	17.6 $\mu\text{m}$ ×	13.0 $\mu\text{m}$ ×	6.6 $\mu\text{m}$ ×	–
		13.2 $\mu\text{m}$ ×	9.7 $\mu\text{m}$ ×	4.9 $\mu\text{m}$ ×	
		13.2 $\mu\text{m}$	9.7 $\mu\text{m}$	4.9 $\mu\text{m}$	

**Fig. 22** Fabrication process cycle of three-layer gradient index anti-reflection structure

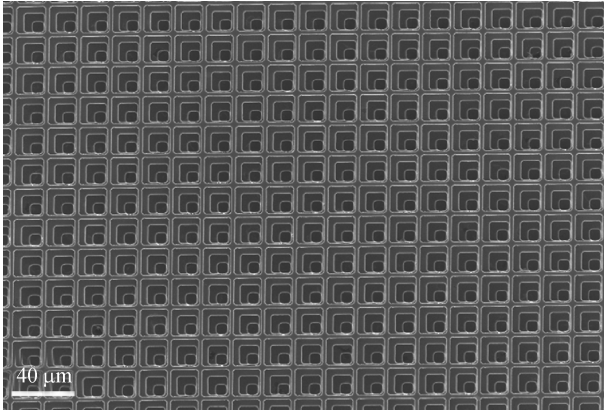


**Fig. 23** SEM image of three-layer gradient index anti-reflection structure with a period of 20  $\mu\text{m}$

substrate, and the largest feature is the layer on the surface. Etched square holes are aligned at the lower right corner. In our design, refractive index of every layer is independent from each other. Therefore, it is not required to have all three layers aligned at a corner or at center. The only requirement is that smaller feature should be inside of larger feature. Good uniformity is achieved across the fabrication area on the substrate.

### 3.4 Performance evaluation

#### 3.4.1 Terahertz time-domain spectroscopy (THz-TDS)

Evaluation of the fabricated anti-reflection structures will utilize a THz-TDS system. THz-TDS has been a widely used method to characterize materials due to the fact that both amplitude and phase information can be obtained through probing with terahertz pulses. Traditionally, a semiconductor surface emitter as such InAs or a photoconductive antenna is used as emitter in THz-TDS. On the other hand, Electro-Optical Sampling or photoconductive antenna is used to detect THz waves. These emitters and detectors have a limited bandwidth up to 5 THz, therefore leaving a large portion of the terahertz frequencies (5 to 10 THz) unexplored. The invention of THz-ABCD technique filled in this gap [16]. For a record-breaking bandwidth from 0.1 to 10 THz, THz-ABCD provides a vehicle for researchers to study materials in almost the entire THz range. The set-up of the THz-ABCD system used for our structure evaluation is shown in Fig. 24 [17] and the specifications of this system are summarized in Table 3.

Before structure evaluation, we first take a reference signal with no sample placed in the terahertz beam path. Figure 25 shows the waveform and Fourier-transformed spectrum of the reference signal. Observing from the spectrum, bandwidth of the system spans from 0.1 to 10 THz. Next we place a high-resistivity silicon ( $\rho > 10 \text{ k}\Omega\text{-cm}$ ) in the sample stage to measure its reflectance. High

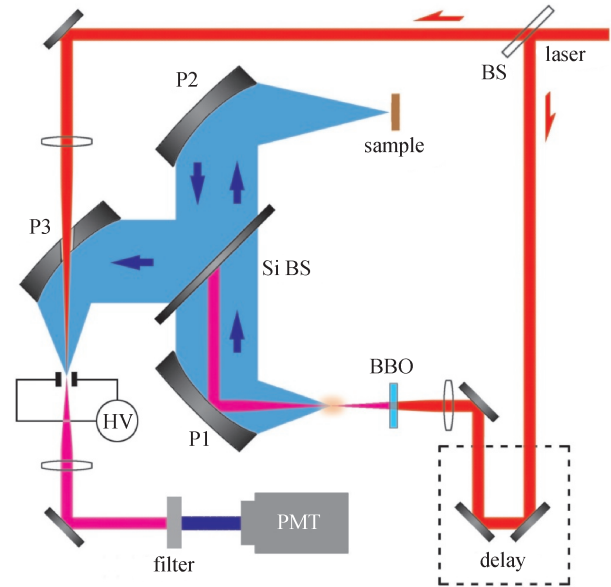


**Fig. 24** THz-ABCD system used for structure evaluation (Si: silicon, BS: beam splitter, P: parabolic mirror, BBO: barium borate crystal, PMT: photomultiplier tube) [17]

**Table 3** THz-ABCD system specification

laser	SP Hurricane amplifier: 1 kHz repetition rate 750 mW power 100 fs pulse duration
terahertz emitter	nitrogen purged
biased electric field	$\sim 20 \text{ kV/cm}$
terahertz receiver	nitrogen purged; fused silica lens
modulation frequency	500 Hz
lock-in time constant	100 ms
measurement type	normal reflection (incident angle: $0^\circ$ )

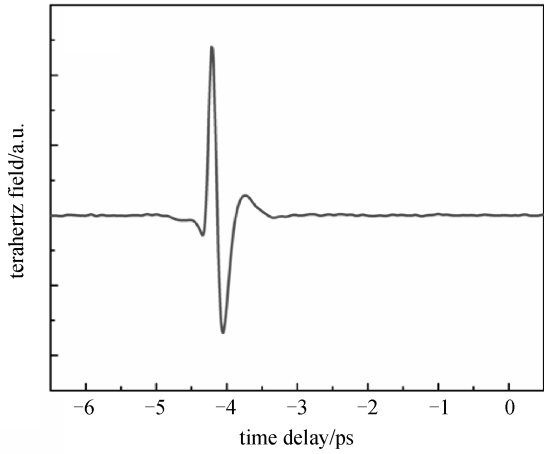
resistivity silicon has a fairly constant relative refractive index ( $\sim 3.42$ ) throughout the terahertz range [18,19]. The reflectance at the air-silicon boundary can be calculated by the following equation,

$$R = \left( \frac{n_{\text{silicon}} - n_{\text{air}}}{n_{\text{silicon}} + n_{\text{air}}} \right)^2, \quad (19)$$

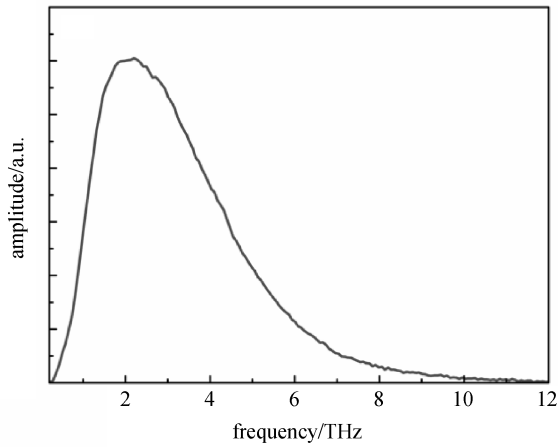
which comes up to be 30%. Figure 26 shows the reflected time-domain waveform of the high-resistivity silicon and its reflectance spectrum. We see good correspondence between our measurement and the theoretical value.

#### 3.4.2 Reflection and transmission evaluation

There are two sets of fabricated structures, one with 20- $\mu\text{m}$  period and the other with 15- $\mu\text{m}$  period. Both samples have a total structure depth of 20- $\mu\text{m}$ . Since 15 and 20  $\mu\text{m}$  are approaching the size of wavelengths at higher frequency range of the system, diffraction will be

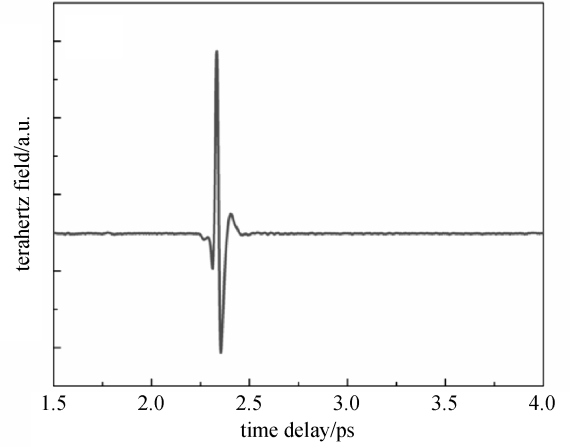


(a)

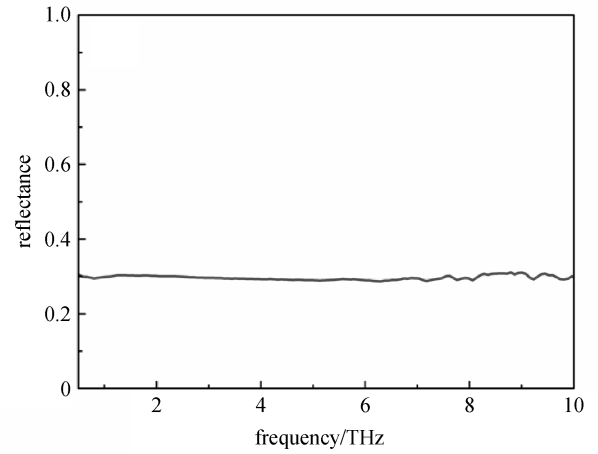


(b)

**Fig. 25** (a) Waveform and (b) spectrum of reference signal of THz-ABCD system



(a)



(b)

**Fig. 26** (a) Reflected waveform and (b) reflectance spectrum of high resistivity silicon

unavoidable. Therefore both reflection and transmission measurements will be carried out in our experiments to give a full picture of the anti-reflection performance of our structures. Figure 27 demonstrates the experiment set-up for structure evaluation.

The first set of experiment is to measure the reflectance of the structures. A reference waveform is taken first without any sample in place. Then a high-resistivity silicon wafer and two samples of three-layer gradient index structures are placed in the sample stage one by one. Their reflected time-domain waveforms are recorded and shown in Fig. 28(a). Significant reduction in reflection can be observed from decreased peak values of the two structures, demonstrating their anti-reflection effect. By taking the Fourier transform of the waveforms, we have the terahertz spectra of these two structures. To obtain a reflectance spectrum, we divide the terahertz spectrum of the structures to that of the reference signal. The results are shown in Fig. 28(b). At low frequencies, the reflectance spectra of both structures closely follow the simulated reflectance. For the 15- $\mu\text{m}$  period gradient index structures,

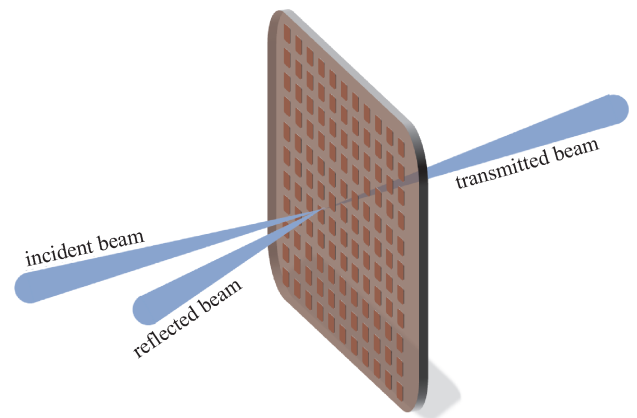


**Fig. 27** Experimental setup of structure evaluation

reflectance is reduced from 30% to less than 5% for the spectral range of 2.2 to 5.5 THz. However, as structure period approaches the size of wavelengths at higher

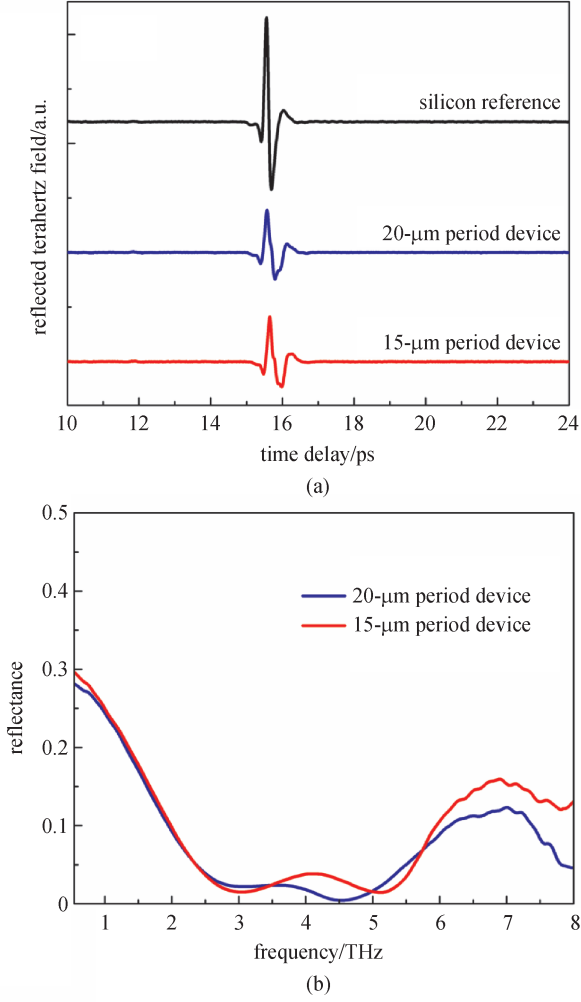


**Fig. 28** Reflection measurement of a 20- $\mu\text{m}$  period and a 15- $\mu\text{m}$  period inverted photonic structure using THz-ABCD- (a) reflected terahertz waveforms and (b) Fourier transform reflectance spectra

frequencies, the structure's anti-reflection effect will decline due to on-set of diffraction. This is because terahertz waves can no longer perceive the structure as a uniform layer-by-layer medium, but rather a rugged structure.

To investigate whether reduction in reflectivity will lead to enhanced transmission, we measure the terahertz waveform in the transmission direction. Experiment results will be analyzed to understand both transmission and diffraction of the three-layer gradient index gratings. Transmitted terahertz time-domain waveforms of planar high-resistivity silicon, a 20- $\mu\text{m}$  period structure and a 15- $\mu\text{m}$  period structure are plotted in Fig. 29(a). Increase of terahertz peak-to-peak values in the waveforms illustrates enhanced transmission of the two fabricated structures. To quantify this enhancement, we compare the Fourier transform spectra of the two structures with that of silicon. The subsequent result is a relative transmission spectrum. Theoretically, relative transmission can be calculated by

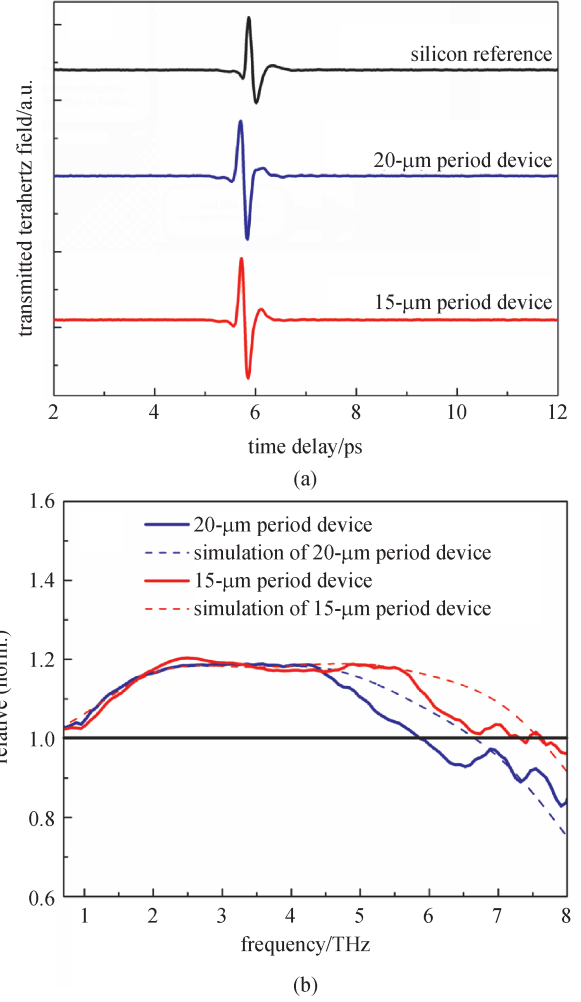


**Fig. 29** Transmission measurement of silicon reference, a 20- $\mu\text{m}$  period and a 15- $\mu\text{m}$  period structure using THz-ABCD- (a) transmitted THz waveforms and (b) relative transmission spectra

the equation

$$t_{\text{relative}} = \sqrt{\frac{1 - R_{\text{structure}}}{1 - R_{\text{silicon}}}}, \quad (20)$$

where  $R_{\text{silicon}}$  can be obtained from Eq. (19) and has a value of 0.3. Under optimal condition,  $R_{\text{structure}}$  will have a value of 0, meaning reflectance is reduced to zero by using a perfect anti-reflection structure. This will yield the upper limit of the relative transmission of any anti-reflection structures, which is approximately 1.195. Figure 29(b) plots the measured relative transmission spectra of the two structures, which is transmission spectrum of the structures normalized to that of silicon. Transmission enhancement is observed in both spectra and it follows precisely with the simulated value until terahertz wavelengths approach the size of the structure period. For a two-dimensional grating, its period has to be small enough for the transmitted wave to be zeroth order diffraction. As the wavelength approach

the grating period, higher order diffraction will start to occur. The wavelength at which first order diffraction appears is defined by

$$\lambda = \Lambda \cdot n_{\text{silicon}}, \quad (21)$$

where  $\Lambda$  is the grating period and  $n_{\text{silicon}}$  is the relative refractive index of silicon [20]. For structure with a 20- $\mu\text{m}$  period, diffraction occurs at 68.4  $\mu\text{m}$  (4.4 THz); for structure with a 15- $\mu\text{m}$  period, diffraction occurs at 51.3  $\mu\text{m}$  (5.8 THz). These two diffraction limits correspond very well with the experimental results shown in Fig. 29(b), as the beginning of the decline in transmission enhancement is observed at these two frequencies for their respective structures. Overall, the anti-reflection bandwidth (transmission enhancement greater than 1) of the 20- $\mu\text{m}$  period structure is from 0.5 to 5.9 THz and that of the 15- $\mu\text{m}$  period structure is from 0.5 to 7.1 THz.

### 3.4.3 Polarization and incident angle measurement

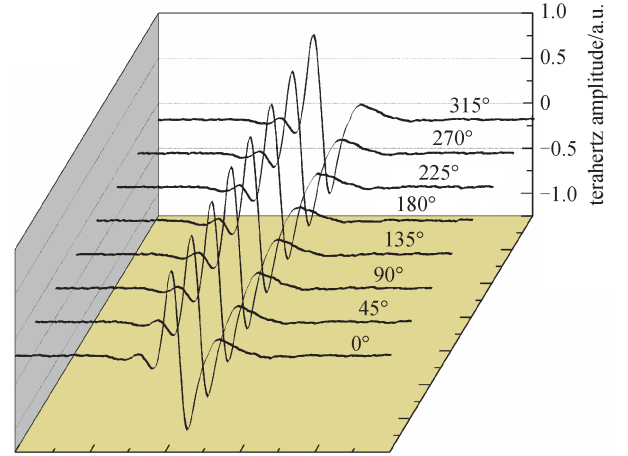
For an anti-reflection structure to be practical and useful, it is desirable to be independent of polarization and incident angle. To further evaluate the gradient index grating, we study its polarization and incident angle dependency. First of all, we take the transmitted terahertz time-domain waveform with the 15- $\mu\text{m}$  period structure at azimuthal angles 0° to 315° in 45° steps, as shown in Fig. 30(a). Then we take the Fourier transform to obtain the spectrum and convert that to relative transmission spectrum. At the end we plot the value at 3.7 THz for all the measurements; the results are shown in Fig. 30(b). We find that the transmission level stays almost the same for all measurements, varying within 2% for all the measurement data. Since the emitted terahertz wave of the THz-ABCD system is p-polarized, we conclude that the anti-reflection structure is polarization independent.

Next, we proceed to evaluate anti-reflection performance of the 15- $\mu\text{m}$  period structures under different incident angles. For p-polarized wave, the reflectance of high resistivity silicon is dependent of incident angle, depicted by Fresnel equation [15].

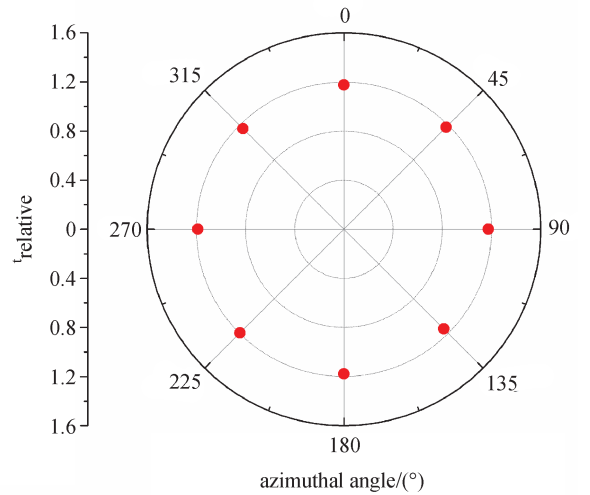
$$R = \frac{n_1 \cdot \sec\theta_1 - n_2 \cdot \sec\theta_2}{n_1 \cdot \sec\theta_1 + n_2 \cdot \sec\theta_2}. \quad (22)$$

As incident angle increases from 0°, reflectance decreases until it reaches zero at 73.7°, known as the Brewster angle. If incident angle continues to increase beyond Brewster angle, reflectance will rise and reach 100% at 90°. This reflectance profile as a function of incident angle for planar silicon is shown in Fig. 31.

In gradient-index design used for the anti-reflection structure, the theory states that the smoothness of refractive angle is the key to insure good anti-reflection performance at a large incident angle. Therefore, the refractive index profile is designed with this objective in mind. To



(a)



(b)

**Fig. 30** (a) Transmitted terahertz waveforms of 15- $\mu\text{m}$  period structure at azimuthal angle from 0° to 315° in 45° steps; (b) relative terahertz transmission amplitude of 15- $\mu\text{m}$  period structure at 3.7 THz

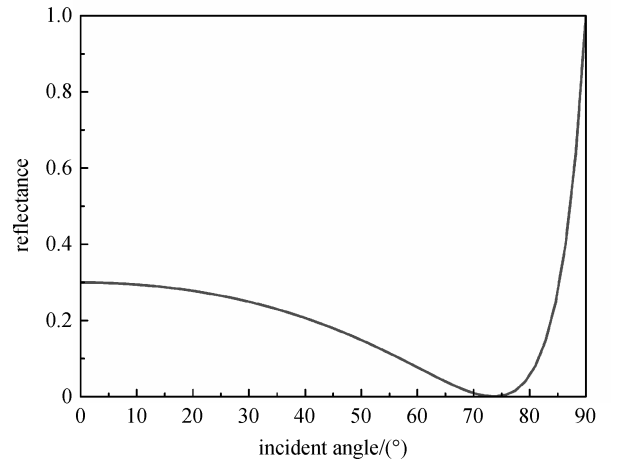


**Fig. 31** Reflectance of p-polarized wave at normal incident on an air to silicon interface

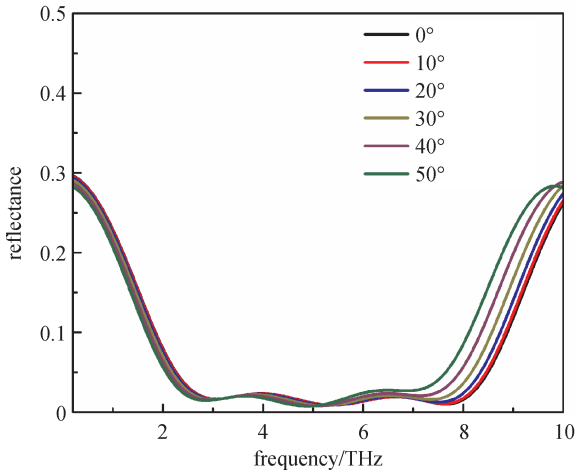
demonstrate the incident angle tolerance of the structure, we modify our model to simulate several cases of different incident angle for TM (p-polarized) wave. Propagation matrix and transmission matrix now have the forms:

$$\mathbf{P}_{(i)} = \begin{bmatrix} e^{-jn_i k d_i \cos \theta_i} & 0 \\ 0 & e^{jn_i k d_i \cos \theta_i} \end{bmatrix}, \quad (23)$$

and

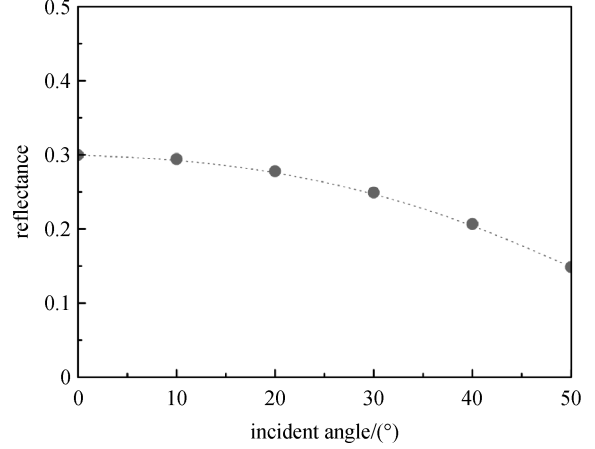
$$\mathbf{T}_{(i)} = \frac{\cos \theta_i}{2 \cdot \cos \theta_{i+1} \cdot n_{i+1} \cdot \sec \theta_{i+1}} \begin{bmatrix} n_{i+1} \cdot \sec \theta_{i+1} + n_i \cdot \sec \theta_i & n_{i+1} \cdot \sec \theta_{i+1} - n_i \cdot \sec \theta_i \\ n_{i+1} \cdot \sec \theta_{i+1} - n_i \cdot \sec \theta_i & n_{i+1} \cdot \sec \theta_{i+1} + n_i \cdot \sec \theta_i \end{bmatrix}. \quad (24)$$

Figure 32 plots the reflectance spectra of the structure under incident angle from  $0^\circ$  to  $50^\circ$  in  $10^\circ$  steps. Observation can be made that only slight changes are shown as incident angle increases from  $0^\circ$  to  $50^\circ$ , with an upper limit of the variation in reflectance of 1.5%. This confirms that the anti-reflection performance of the structures can tolerate a large incident angle. On the other hand, we also model the reflectance spectra of planar silicon at different incident angle at 3.7 THz for comparison. The results are shown in Fig. 33. Decrease in reflectance is dramatic at larger incident angles. For example, reflectance drops to half at 15% with a  $50^\circ$  incident angle compared to 30% at normal incidence.



**Fig. 32** Simulated reflectance spectra of three-layer gradient index structure at different incident angle

In the THz-ABCD system, reflection evaluation has a stricter requirement for sample position because it has to be placed at the focal point of the terahertz beam whereas transmission evaluation only requires sample to be placed at the terahertz beam path. In the system we used for



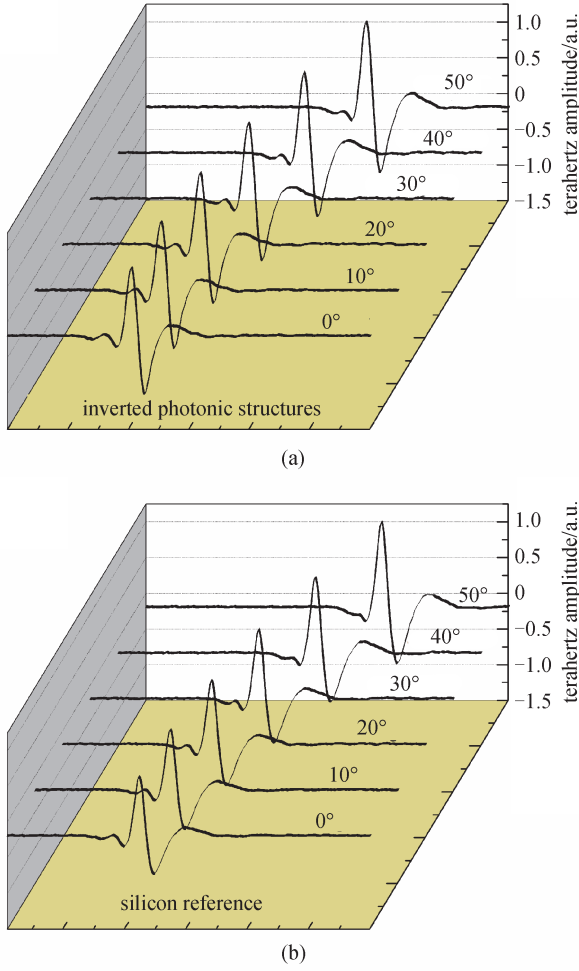
**Fig. 33** Simulated reflectance spectra of planar silicon at different incident angle at 3.7 THz

structure evaluation, a mirror holder is fixed at the focal point of the terahertz beam to insure repeatable results time after time. To have reflection measurement for varies incident angle on the structure, it will require removal of the mirror holder and intensive alignment work during and after structure evaluation. To avoid alteration of the THz-ABCD system, we choose transmission measurement, which can also give us a quantitative result on wide incident angle performance of the structures. For each incident angle, two transmitted terahertz time-domain waveforms are recorded: one for the structure and one for planar silicon. They are shown in Fig. 34. When incident angle increases from  $0^\circ$  to  $50^\circ$ , amplitude of the transmitted terahertz waveform also increases for both the 15- $\mu\text{m}$  period structure and silicon reference. For each incident angle, we also notice that the waveform of the 15- $\mu\text{m}$  period structure has a larger amplitude than that of silicon reference.

After converting the transmitted time-domain waveforms into spectra, the spectrum of the structure is divided by that of the planar silicon to obtain the relative transmission spectrum. Measurements are performed for incident angles from  $0^\circ$  to  $50^\circ$ , in  $10^\circ$  steps. For simulation, transmission spectra of the structure and planar silicon are calculated for the same set of incident angles. Simulated relative transmission spectrum is then obtained by dividing the transmission spectrum of the structure to that of the planar silicon. Figure 35 shows the experiment results (dash curve in red) along with simulated results (solid curve in black). Overall, measured relative transmission spectra are in good agreement with simulated results and transmission enhancement maintains above 1 throughout the frequency range of 0.5 to 5.5 THz.

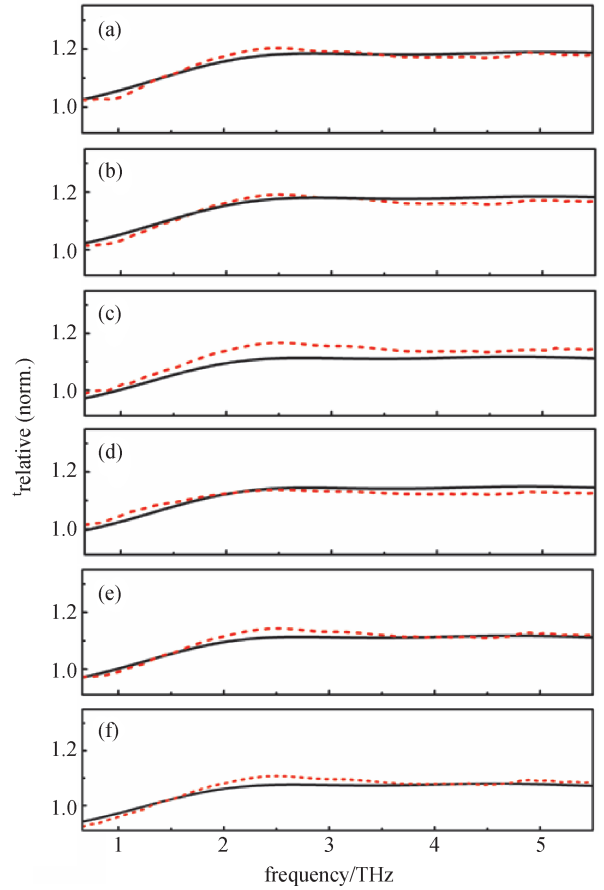
#### 3.4.4 Design sensitivity

Photo mask production and mask pattern transfer are two main reasons that can cause the final structure dimensions



**Fig. 34** Transmitted terahertz waveforms of (a) 15- $\mu\text{m}$  period structure and (b) silicon reference at incident angles from 0° to 50°

to deviate from the original design. To insure anti-reflection effect of the fabricated structures, it is important to analyze the performance of the structure with slightly altered dimensions. To cover a reasonable range of variation, for each layer we assume there is a  $\pm 5\%$  differences between the fabricated hole-dimension and the original design. Table 4 shows a summary of the parameters and their corresponding relative refractive indices. From the six generated parameters ( $n_{2,0}$ ,  $n_{2,1}$ ,  $n_{3,0}$ ,  $n_{3,1}$ ,  $n_{4,0}$ ,  $n_{4,1}$ ), where the first subscript indicates the layer and the second subscript indicates positive or negative discrepancy. There are a total of eight combinations, as shown in Fig. 36. For each combination we plot a simulated reflectance spectrum and they are compared to the original simulated reflectance spectrum. The results are shown in Fig. 37. We notice that deviation of hole dimensions will lead to slight degradation in anti-reflection performance of the structure. Since hole dimension is largest in layer 2, a 5% discrepancy will lead to a greater fluctuation of relative refractive index in layer 2 than that in



**Fig. 35** Simulated (solid curve in black) and measured (dash curve in red) relative transmission spectra of three-layer gradient index structure at various incident angles: (a) 0°, (b) 10°, (c) 20°, (d) 30°, (e) 40°, (f) 50°

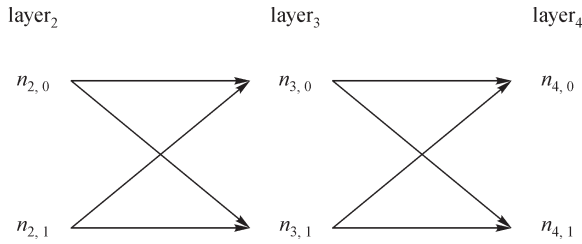
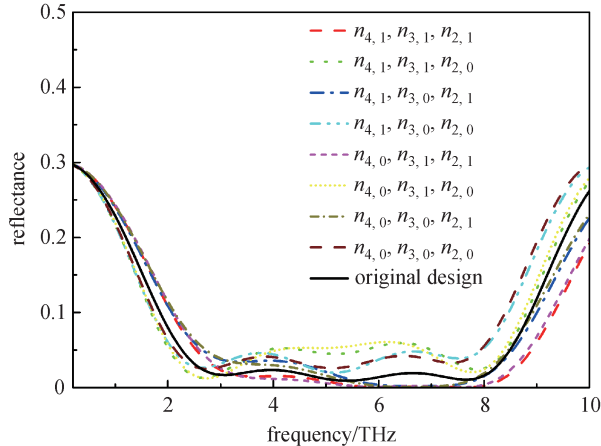
layers 3 and 4. Therefore, variation in layer 2 hole dimension will have a larger impact on anti-reflection performance than that in layers 3 and 4. When the relative refractive index of layer 2 is decreased from the original value of 1.55, reflectance will remain very low from 3 to 8 THz. Hence, a tight control on layer 2 dimension is the key to attain a good anti-reflection profile.

### 3.4.5 Five-layer and seven-layer gradient index designs

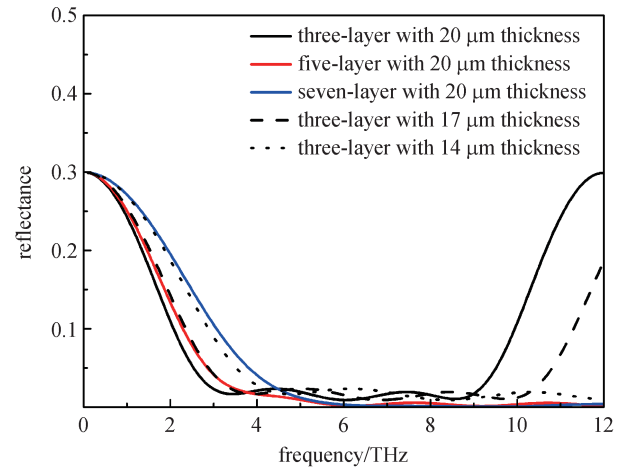
Due to fabrication complexity, we choose a three-layer gradient index design over five-layer and seven-layer designs. Nonetheless, it is valuable to compare the anti-reflection performance of these three designs to justify performance scarification over design complication. In Fig. 38, the simulated reflectance of a three-layer, a five-layer and a seven-layer design are compared. The simulated reflectance is first obtained using the same unit wavelength (same overall structure thickness of 20  $\mu\text{m}$ ) for all three designs. Although a five-layer and a seven-layer design have boarder anti-reflection bandwidth, a three-layer

**Table 4** Summary of parameters with their corresponding relative refractive indices

	original design	-5% discrepancy	+5% discrepancy
layer 2	$a_2 = 13.2 \mu\text{m}$ , $n_2 = 1.55$	$a_{2,0} = 12.54 \mu\text{m}$ , $n_{2,0} = 1.70$	$a_{2,1} = 13.86 \mu\text{m}$ , $n_{2,1} = 1.37$
layer 3	$a_3 = 9.7 \mu\text{m}$ , $n_3 = 2.25$	$a_{3,0} = 9.22 \mu\text{m}$ , $n_{3,0} = 2.33$	$a_{3,1} = 10.19 \mu\text{m}$ , $n_{3,1} = 2.17$
layer 4	$a_4 = 4.9 \mu\text{m}$ , $n_4 = 2.95$	$a_{4,0} = 4.66 \mu\text{m}$ , $n_{4,0} = 2.98$	$a_{4,1} = 5.15 \mu\text{m}$ , $n_{4,1} = 2.92$

**Fig. 36** Combinations of parameter variation for design sensitivity analysis**Fig. 37** Simulated reflectance of inverted photonic structure with variations on hole dimension in each layer

structure has smaller low frequency reflectance. Therefore, a five-layer and a seven-layer structure will need to have a larger structure thickness to achieve the same reflectance as a three-layer design below 3 THz. This can make the fabrication process more challenging. For comparison, we also plotted the three-layer design with decreased structure thickness of 17 and 14  $\mu\text{m}$ . As structure thickness decreases, the anti-reflection profile of the three-layer design will have an expansion in bandwidth. When structure thickness reduced to 14  $\mu\text{m}$ , the overall reflectance profile of the three-layer design is comparable to that of the seven-layer design with a structure thickness of 20  $\mu\text{m}$ .

**Fig. 38** Simulated reflectance of three-layer, five-layer and seven-layer inverted photonic designs

## 4 Conclusions

Anti-reflection implementation can be carried out using different methods. Quarter-wave coating, absorptive layer coating, multi-layer coating, meta-materials design and sub-wavelength surface relief structure design have been used in the past to reduce reflection at the interface of air to high-index substrate in the terahertz range.

Our approach to anti-reflection implementation is based on gradient-index anti-reflection theory. We use DRIE to remove certain percentage of silicon to form a layer with an engineerable refractive index, which can be calculated by a capacitor model. To have fast fabrication turnover time, a three-layer design is chosen. We fabricated two sets of structure, one with 20- $\mu\text{m}$  structure period and one with 15- $\mu\text{m}$  structure period; both structures have a total depth of 20- $\mu\text{m}$ . To evaluate the anti-reflection performance of these structures, we use a THz-ABCD system, which has a usable bandwidth from 0.5 to over 10 THz. Reflection measurement and transmission measurement are performed individually for a comprehensive assessment. Measurement result shows that both structures can reduce reflection from 30% to lower than 5% over a wide range of frequencies. Enhanced transmission is observed from 0.5

to 5.9 THz for the 20- $\mu\text{m}$  period structure and from 0.5 to 7.1 THz for the 15- $\mu\text{m}$  period structure. Polarization measurement and incident angle measurement are carried out subsequently to assess the versatility of the three-layer gradient index structures. It is found that, these structures are polarization independent. They are also suitable to be used under an incident angle up to  $50^\circ$  without imposing considerable damage on their anti-reflection effect.

Our implementation of terahertz anti-reflection on silicon using gradient index structure design can be easily tuned to apply for other wavelengths. For example, by reducing the structure period and depth to a few microns or a few hundred nanometer, these structures can be used in the near and mid infrared region. Furthermore, this design can also be applied to other materials, such as germanium and gallium arsenide. By using standard CMOS processes, we can achieve low-cost production, high throughput and great reliability for structure fabrication.

## References

- Englert C R, Birk M, Maurer H. Antireflection coated, wedged, single-crystal silicon aircraft window for the far-infrared. *IEEE Transactions on Geoscience and Remote Sensing*, 1999, 37(4): 1997–2003
- Gatesman A J, Waldman J, Ji M, Musante C, Yangvesson S. An anti-reflection coating for silicon optics at terahertz frequencies. *IEEE Microwave and Guided Wave Letters*, 2000, 10(7): 264–266
- McKnight S W, Stewart K P, Drew H D, Moorjani K. Wavelength-independent anti-interference coating for the far-infrared. *Infrared Physics*, 1987, 27(5): 327–333
- Kröll J, Darmo J, Unterrainer K. Metallic wave-impedance matching layers for broadband terahertz optical systems. *Optics Express*, 2007, 15(11): 6552–6560
- Thoman A, Kern A, Helm H, Walther M. Nanostructured gold films broadband terahertz antireflection coating. *Physical Review B: Condensed Matter and Materials Physics*, 2008, 77(19): 195405
- Poitras D, Dobrowolski J A. Toward perfect antireflection coatings. 2. Theory. *Applied Optics*, 2004, 43(6): 1286–1295
- Hosako I. Multilayer optical thin films for use at terahertz frequencies: method of fabrication. *Applied Optics*, 2005, 44(18): 3769–3773
- Chen H T, Zhou J, O'Hara J F, Chen F, Azad A K, Taylor A J. Antireflection coating using metamaterials and identification of its mechanism. *Physical Review Letters*, 2010, 105(7): 073901
- Brückner C, Pradarutti B, Stenzel O, Steinkopf R, Riehemann S, Notni G, Tünnermann A. Broadband antireflective surface-relief structure for THz optics. *Optics Express*, 2007, 15(3): 779–789
- Kuroo S, Shiraishi K, Sasho H, Yoda H, Muro K. Triangular surface-relief grating for reduction of reflection from silicon surface in the 0.1–3 terahertz region. In: *Proceedings of CLEO/Quantum Electronics and Laser Science Conference and Photonic Applications Systems Technologies*. 2008, CThD7
- Chen Y W, Han P Y, Zhang X C. Tunable broadband antireflection structures for silicon at terahertz frequency. *Applied Physics Letters*, 2009, 94(4): 041106
- Dobrowolski J A, Poitras D, Ma P, Vakil H, Acree M. Toward perfect antireflection coatings: numerical investigation. *Applied Optics*, 2002, 41(16): 3075–3083
- Chen M, Chang H C, Chang A S P, Lin S Y, Xi J Q, Schubert E F. Design of optical path for wide-angle gradient-index antireflection coatings. *Applied Optics*, 2007, 46(26): 6533–6538
- Kadlec C, Kadlec F, Kuzel P, Blary K, Mounaix P. Materials with on-demand refractive indices in the terahertz range. *Optics Letters*, 2008, 33(19): 2275–2277
- Saleh B E A, Teich M C. *Fundamentals of Photonics*, New Jersey: Wiley, 2007, 246–251
- Dai J, Xie X, Zhang X C. Detection of broadband terahertz waves with a laser-induced plasma in gases. *Physical Review Letters*, 2006, 97(10): 103903
- Ho I C, Guo X, Zhang X C. Design and performance of reflective terahertz air-biased-coherent-detection for time-domain spectroscopy. *Optics Express*, 2010, 18(3): 2872–2883
- Dai J, Zhang J, Zhang W, Grischkowsky D. Terahertz time-domain spectroscopy characterization of the far-infrared absorption and index refraction of high-resistivity, float-zone silicon. *Journal of the Optical Society of America. B, Optical Physics*, 2004, 21(7): 1379–1386
- Loewenstein E V, Smith D R, Morgan R L. Optical constants of far infrared materials. 2: crystalline solids. *Applied Optics*, 1973, 12(2): 398–406
- Brückner T, Käsebier T, Pradarutti B, Riehemann S, Notni G, Kley E B, Tünnermann A. Broadband antireflective structures applied to high resistive float zone silicon in the THz spectral range. *Optics Express*, 2009, 17(5): 3063–3077



**Yuting W. Chen** received the B.S. degree in electrical engineering from the University of Illinois–Urbana Champaign in 2007, the M. S. and Ph.D. degrees in electrical engineering from Rensselaer Polytechnic Institute (RPI) in 2009 and 2011, respectively. During her graduate study, she was a National Science Foundation IGERT Fellow in the Center for Terahertz Research at RPI. Her research was in the area of silicon photonic structures for broadband anti-reflection of terahertz waves. She was the recipient of the Founders Award of Excellence at RPI in 2009 and holds two U.S. patents. Dr. Chen is currently with IBM at Poughkeepsie, NY.



**Xi-Cheng Zhang**–Parker Givens Chair of Optics, assumes Directorship of The Institute of Optics, University of Rochester (UR), NY, a foremost institution in optics and optical physics research and education, on 1/1/2012. Prior to joining UR, he pioneered world-leading research in the field of ultrafast laser-based terahertz technology and optical physics at Rensselaer Polytechnic Institute (RPI), Troy NY (1992–2012). At RPI, he is the Eric Jonsson

Professor of Science; Acting Head at the Department of Physics, Applied Physics & Astronomy; Professor of Electrical, Computer & System; and Founding Director of the Center for THz Research. He is co-founder of Zomega Terahertz Corp. With a B.S. (1982) from Peking University, he earned the M.S. (1983) and Ph.D. degree (1985) in Physics from Brown University, RI.

Previous positions included Visiting Scientist at MIT (1985), Physical Tech. Division of Amoco Research Center (1987), EE Dept. at Columbia University (1987–1991); Distinguished Visiting Scientist at Jet Propulsion Lab, Caltech (2006). He holds 27 U.S. patents, and is a prolific author and speaker. He is a Fellow of AAAS, APS (lifetime), IEEE, and OSA (lifetime). Dr. Zhang served as Editor-in-Chief of Optics Letters (2014 – 2016).

His honors and awards include: IRMMW-THz Kenneth Button Prize (2014); OSA William F. Meggers Award (2012); IEEE Photonics Society William Streifer Scientific Achievement Award (2011); Rensselaer William H. Wiley 1866 Award (2009); Japan Society for the Promotion of Science Fellowship & NRC-CIAR Distinguished Visiting Scientist, Ottawa, Canada (2004); and First Heinrich Rudolf Hertz Lecturer, RWTH, Aachen, Germany (2003). He also served two years as a Distinguished Lecturer of IEEE/LEOS. He received Rensselaer Early Career Award (1996), Research Corporation Cottrell Scholar Award (1995), NSF Early Career Award (1995), K.C. Wong Prize, K.C. Wong Foundation, Hong Kong (1995), NSF Research Initiation Award (1992). In 1993–1994, he was an AFOSR-SRPF Fellow at Hanscom Air Force Base.